DOI: 10.1002/smtd.202201598
Article type: Full Paper

Double-Transition-Metal MXene Films Promoting Deeply Rechargeable Magnesium Metal Batteries

*Yuanjian Li, Wei Ying Lieu, Tanmay Ghosh, Lin Fu, Xiang Feng, Andrew Jun Yao Wong, Anupma Thakur, Brian C. Wyatt, Babak Anasori, Qianfan Zhang, Hui Ying Yang, Zhi Wei Seh**

Dr. Y. Li, W. Y. Lieu, Dr. T. Ghosh, A. J. Y. Wong, Prof. Z. W. Seh
Institute of Materials Research and Engineering, Agency for Science, Technology and Research (A*STAR), 2 Fusionopolis Way, Innovis, Singapore 138634, Singapore
E-mail: sehzw@imre.a-star.edu.sg

W. Y. Lieu, Prof. H. Y. Yang
Pillar of Engineering Product Development, Singapore University of Technology and Design, 8 Somapah Road, Singapore 487372, Singapore

Dr. L. Fu
School of Chemistry and Chemical Engineering, Guizhou University, Guiyang, Guizhou, 550025, P. R. China

X. Feng, Prof. Q. Zhang
School of Materials Science and Engineering, Beihang University, Beijing 100191, P. R. China

Dr. A. Thakur, B. C. Wyatt, Prof. B. Anasori
Department of Mechanical and Energy Engineering and Integrated Nanosystems Development Institute, Purdue School of Engineering and Technology, Indiana University-Purdue University Indianapolis, Indianapolis 46202, USA

Keywords: MXene**,** magnesium metal batteries, magnesium plating/stripping, high capacity, deep cycling

Magnesium (Mg) metal batteries are promising candidates for next-generation high-energy-density and low-cost energy storage systems. Their application, however, is precluded by infinite relative volume changes and inevitable side reactions of Mg metal anodes. These issues become more pronounced at large areal capacities that are required for practical batteries. Herein, for the first time, double-transition-metal MXene films are developed to promote deeply rechargeable magnesium metal batteries using $Mo_2Ti_2C_3$ as a representative example. The freestanding $Mo_2Ti_2C_3$ films, which are prepared using a simple vacuum filtration method,

possess good electronic conductivity, unique surface chemistry, and high mechanical modulus. These superior electro-chemo-mechanical merits of $Mo_2Ti_2C_3$ films help to accelerate electrons/ions transfer, suppress electrolyte decomposition and dead Mg formation, as well as maintain electrode structural integrity during long-term and large-capacity operation. As a result, the as-developed $Mo_2Ti_2C_3$ films exhibit reversible Mg plating/stripping with high Coulombic efficiency of 99.3% at a record-high capacity of 15 mAh cm^{-2}. This work not only sheds innovative insights into current collector design for deeply cyclable Mg metal anodes, but also paves the way for the application of bimetallic MXene materials in other alkali and alkaline earth metal batteries.

1. Introduction

Rechargeable magnesium metal batteries (RMBs) are recognized as promising candidates for next-generation high-energy-density and cost-effective energy storage devices due to the advantages of metallic Mg, including high volumetric capacity (3833 mAh cm^{-3}), low redox potential (-2.37 V vs. standard hydrogen electrode), and abundant resources.[1] However, the practical application of Mg metal anode in conventional electrolytes faces two primary issues. First, the low redox potential makes magnesium metal react readily with electrolyte salts and solvents to produce ionic-insulating passivating layers on the anode surface, which gives rise to irreversible plating/stripping behavior.[2] Second, owing to its "hostless" nature, the Mg metal anode undergoes infinite relative volume expansion/shrinkage during the charge/discharge process, inevitably causing repeated fracture/repair of surface passivation layers.[3] As a result, active magnesium and electrolytes are being progressively consumed, eventually resulting in premature battery failure with low Coulombic efficiency and poor cyclability.

Massive efforts have been devoted to circumventing the critical issues in magnesium metal batteries. For example, manipulating electrolyte compositions through the use of chlorinated

additives,[4] chloride-free ligands,[5] weakly coordinating anions,[6] and chelates[7] could help to form robust solid electrolyte interphase (SEI) layers on Mg anode surface. Artificial SEI layers, including inorganic compounds,[8] organic polymers,[9] and their hybrids,[10] are effective in permitting Mg ion conduction and avoiding Mg anode passivation by electrolytes. However, owing to their poor mechanical properties, most SEI layers are prone to be detached in the case of large anode capacities encountered during the deep cycling of practical batteries, which suffer from large volume fluctuation.[11] Recently, three-dimensional (3D) magnesiophilic current collectors have attracted great attention in Mg metal batteries as they can provide a large specific surface area to accommodate volume variations during cycling.[12] For example, Cui and co-workers designed vertically aligned nitrogen- and oxygen-doped carbon nanofiber arrays on carbon cloth (VNCA@C) that exhibited strong magnesium affinity to guide smooth Mg deposition even at high capacities of 8 mAh cm^{-2}.[13] Most of these works focus on enhancing the magnesiophilicity of current collectors to promote uniform Mg deposition. However, the impact of other electro-chemo-mechanical properties of current collectors remains relatively unknown, and ultrahigh magnesium plating/stripping capacity (≥ 10 mAh cm^{-2}) has therefore not been achieved.

Two-dimensional (2D) transition metal carbides (MXenes), which possess high electrical conductivity, large surface area, and tunable surface functional groups (-OH, -O, and -F), are being widely used in many fields, including in rechargeable batteries.[14] For example, MXenes have been explored as high-performance current collectors for lithium metal anodes, such as 3D porous MXene aerogels,[15] parallelly aligned MXene layers,[16] vertically aligned MXene nanosheet arrays,[17] and so on.[18] However, these works mainly focus on single-transition-metal MXenes, particularly titanium carbides (Ti_3C_2). In the case of Mg metal anodes, MXenes have not been reported before as current collectors for Mg plating/stripping to the best of our knowledge. Some recent advances found that double-transition-metal MXenes exhibit more unique electronic structures, stronger metal-philicity, and higher mechanical strength than the

Ti_3C_2 MXene.[19] Therefore, it would be highly desirable, yet challenging, to develop bimetallic MXenes with superior electro-chemo-mechanical properties to improve the Mg plating/stripping reversibility for deeply rechargeable Mg metal batteries.

Herein, for the first time, we report the development of a classic bimetallic $Mo_2Ti_2C_3$ MXene as freestanding films to successfully meet the practical demands of deeply rechargeable magnesium metal batteries. Systematic investigations demonstrate multilevel advantages of $Mo_2Ti_2C_3$ film over its Ti_3C_2 counterpart, including: (1) larger interlayer spacing (1.65 vs 1.45 nm) to facilitate Mg^{2+} rapid diffusion, (2) more desirable surface terminations (more -O, and less -F) to reduce Mg nucleation energy barrier and suppress active magnesium and electrolyte consumption during long-term cycling, (3) better electronic conductivities (3.62×10^2 vs 1.82×10^2 S m^{-1}) to decrease the charge transfer resistance during Mg plating/stripping, and (4) higher Young's modulus (3.5 vs 2.2 GPa) to withstanding the compressive stress and electrode volumetric change during large capacity operation. Benefitting from these electro-chemo-mechanical advantages, the as-obtained $Mo_2Ti_2C_3$ film achieve reversible Mg plating/stripping cycling with high Coulombic efficiency of 99.3% at an ultra-large capacity of 15 mAh cm^{-2}, whereas the Ti_3C_2 film cannot work under the same conditions. These results demonstrate great promise for implementing double-transition-metal MXene ($Mo_2Ti_2C_3$) materials in practical Mg metal batteries.

2. Results and Discussion

Figure S1 schematically illustrates the fabrication procedure of $Mo_2Ti_2C_3$ film. Typically, $Mo_2Ti_2C_3$ nanosheets (Figure S2, Supporting Information) are synthesized by selectively removing Al from $Mo_2Ti_2AlC_3$ with hydrofluoric acid.[19b] After further delamination in tetramethylammonium hydroxide (TMAOH) solution, high-quality single-layered $Mo_2Ti_2C_3$ nanosheets were collected, as confirmed by the transmission electron microscopy (TEM) image

(Figure 1a). The high-angle annular dark-field scanning TEM (HAADF-STEM) image and the corresponding elemental mappings (Figure 1b) demonstrate the homogeneous distribution of molybdenum, titanium, carbon, fluorine, and oxygen elements in the $Mo_2Ti_2C_3$ nanosheets. The extensive F and O signals are likely to arise from surface termination groups like -F, -OH, and -O, which are chemically introduced onto the $Mo_2Ti_2C_3$ surface during the etching process. For comparison, we also prepared Ti_3C_2 nanosheets through a similar process with the Ti_3AlC_2 precursor (Figure S3, Supporting Information). To compare the structural differences between Ti_3C_2 and $Mo_2Ti_2C_3$ nanosheets, X-ray diffraction (XRD) was conducted. In the XRD patterns (Figure 1c, d, Figure S4, Supporting Information), the (002) peak of $Mo_2Ti_2C_3$ nanosheets exhibits a lower 2θ value than that of Ti_3C_2 nanosheets (5.36° vs 6.07°), signifying an increase in $Mo_2Ti_2C_3$ interlayer spacing (1.65 vs 1.45 nm), which is expected to expedite Mg ion transport during the plating/stripping process.[14a]

Freestanding Ti_3C_2 and $Mo_2Ti_2C_3$ films (insets of Figure 1e and g) were thereafter obtained through the vacuum filtration of Ti_3C_2 and $Mo_2Ti_2C_3$ suspensions respectively. The morphological features of Ti_3C_2 and $Mo_2Ti_2C_3$ films were monitored by scanning electron microscopy (SEM) images. Both the Ti_3C_2 (Figure 1e and S5, Supporting Information) and $Mo_2Ti_2C_3$ films (Figure 1g and S6, Supporting Information) are observed to have rough and wrinkled surfaces due to the overlap of MXene nanosheets during the filtration process.[18b] The cross-sectional SEM images reveal that $Mo_2Ti_2C_3$ film exhibits a compact structure (Figure 1h), which contrasts with the typical porous structure of Ti_3C_2 film (Figure 1f). Although the porous Ti_3C_2 film can offer a large open surface area to accommodate magnesium metal, it also aggravates the side reactions with liquid electrolytes, which is detrimental to long-term cycling stability.[15] In addition, the thickness of $Mo_2Ti_2C_3$ film (~ 32 μm) is remarkably reduced compared to Ti_3C_2 film (~ 60 μm), potentially due to $Mo_2Ti_2C_3$ flakes having higher densities,

demonstrates another significant advantage of $Mo_2Ti_2C_3$ films as current collectors in high-volumetric-energy-density Mg metal batteries.

X-ray photoelectron spectroscopy (XPS) measurements were performed to further analyze the surface chemical properties of $Mo_2Ti_2C_3$ films. The Mo 3d, Ti 2p, and C 1s XPS spectra shown in Figure S7a-c (Supporting Information) demonstrate the presence of C-Mo^{4+}, C-Ti^{+}, C-Ti^{2+}, and C-Ti^{3+} bonds in $Mo_2Ti_2C_3$ film, in agreement with previous reports.[20] Other surface termination groups like -F, -OH, and -O are also found in the O 1s and F 1s spectra (Figure S7d and e, Supporting Information), consistent with the above EDX mapping. According to the XPS results of $Mo_2Ti_2C_3$ film, the atomic percentages of the Mo, Ti, C, O, and F elements are estimated to be 7.4, 5.9, 67.3, 16.7, and 2.7 at% respectively. Figure 2a and S8 (Supporting Information) also give the atomic percentage of 22.2, 55.8, 12.2, and 9.8 at% for Ti, C, O, and F elements in the Ti_3C_2 film, respectively. Due to the weaker bond strength of Mo-F compared to Ti-F, the $Mo_2Ti_2C_3$ MXenes are found to have very low F basal plane coverages and more O basal plane coverages than Ti_3C_2 MXenes. [19d] While previous reports have demonstrated the effectiveness of surface fluorine termination groups in forming durable fluorinated SEI layers,[18c] massive amounts of F-terminated groups on the surface of Ti_3C_2 can cause a large consumption of active Mg to form SEI during the initial deposition, subsequently decreasing reversible Mg amounts during dissolution.[15] It is also worth noting that O-terminated MXene usually has higher binding energies with metal atoms (Li, Na, and K) than the F-terminated one.[21] Therefore, $Mo_2Ti_2C_3$ possesses a significant advantage over Ti_3C_2 by providing a higher density of surface oxygen terminations that can better adsorb magnesium atoms and reduce its nucleation energy barrier, thus helping to homogenize Mg plating/stripping behavior.

Nanoindentation tests were performed to investigate the mechanical properties of Ti_3C_2 and $Mo_2Ti_2C_3$ films. Force-displacement curves in Figure 2b display that Young's modulus of $Mo_2Ti_2C_3$ film reaches 3.5 GPa, which is much higher than the 2.2 GPa of Ti_3C_2 film under the same conditions. The stiffer $Mo_2Ti_2C_3$ film is expected to buffer the high stress caused by the

large volume expansion/shrinkage encountered during the large capacity plating/stripping cycling.[22] Besides the high mechanical modulus, high electronic conductivity is also essential for successful current collectors as it can decrease the charge transfer resistance and overpotential for metal deposition.[14b, 23] To investigate the electronic conductivity of Ti_3C_2 and $Mo_2Ti_2C_3$ films, polarization I-V curves of symmetric cells were performed. As presented in Figure 2c, the electronic conductivity of Ti_3C_2 and $Mo_2Ti_2C_3$ films are determined to be 3.62×10^2 and 1.82×10^2 S m^{-1} respectively.The higher conductivity of $Mo_2Ti_2C_3$ film stems from its higher film density and better interfacial contact between the stacked layers.[14c]

To evaluate the electrochemical properties of the $Mo_2Ti_2C_3$ film, asymmetrical Mg coin-type cells were assembled using a conventional magnesium triflate ($Mg(OTf)_2$) based ether electrolyte.[4b] Figure 2d compares the cyclic voltammetry (CV) curves of Mg||Ti_3C_2 and Mg||$Mo_2Ti_2C_3$ cells at a scan rate of 5 mV s^{-1}. A pair of cathodic and anodic peaks are found on both Ti_3C_2 and $Mo_2Ti_2C_3$ films, which corresponds to the Mg plating/stripping process and agree well with previous reports.[24] Moreover, the $Mo_2Ti_2C_3$ film exhibits lower onset potentials and higher current responses during both cathodic and anodic sweeps than the Ti_3C_2 film, implying more favorable Mg plating/stripping kinetics on the $Mo_2Ti_2C_3$ film. The Nyquist plots derived from electrochemical impedance spectroscopy (EIS) measurements (Figure 2e) also support the CV results, where the $Mo_2Ti_2C_3$ film exhibits a much smaller charge transfer resistance (R_{ct}) than the Ti_3C_2 film (37.9 kΩ vs 200 kΩ). The other thing to note is that the bulk resistance experiences a decline from 477.5 Ω to 416 Ω by replacing Ti_3C_2 with $Mo_2Ti_2C_3$. These two reduced resistances reveal that the $Mo_2Ti_2C_3$ film can boost both electronic and ionic transport kinetics in a working Mg metal battery.[25]

The excellent electro-chemo-mechanical properties of $Mo_2Ti_2C_3$ films inspire us to further evaluate their advantages for regulating the electrochemical performance of RMBs. Galvanostatic magnesium plating and stripping measurements were carried out on the Ti_3C_2 and $Mo_2Ti_2C_3$ films at a current density of 3 mA cm^{-2} with a fixed discharge capacity of 3 mA

h cm^{-2} and a cutoff charge voltage of 1.2 V. As shown in Figure 2f, the $Mo_2Ti_2C_3$ film exhibits a lower magnitude of nucleation overpotential (≈ -2.07 V) than that of Ti_3C_2 film (≈ -2.21 V) in the initial plating process. This is probably due to the abundant oxygen groups on the surface of $Mo_2Ti_2C_3$ film, which can serve as magnesiophilic sites to decrease the Mg nucleation barrier. In addition, the initial CE for $Mo_2Ti_2C_3$ film reaches 91.6 %, much higher that for Ti_3C_2 (90.9 %), suggesting that the $Mo_2Ti_2C_3$ film effectively suppresses the consumption of active magnesium during the SEI formation process. Figure 2g shows that the CE of $Mo_2Ti_2C_3$ film rises to 99.5% at the 2nd cycle and continues to be larger than 99.0% in the following 220 cycles. In contrast, the Ti_3C_2 film survives only 180 cycles and the CE suffers a sharp drop to 61%. This inferior CE stability of Ti_3C_2 film is potentially caused by the gradually increased overpotential during cycling, as observed from the charging/discharging voltage profiles and the Nyquist plots (Figure S9 and S10, Supporting Information).

The plating and stripping reversibility of Mg||Ti_3C_2 and Mg||$Mo_2Ti_2C_3$ cells were further evaluated according to the Aurbach Coulombic efficiency (CE) test.[26] As shown in Figure 2h, a capacity of 10 mAh cm^{-2} was first electrochemically plated and then stripped to 1.0 V before depositing the Mg reservoir (Q_T =10 mAh cm^{-2}) on the Ti_3C_2 and $Mo_2Ti_2C_3$ films at a current density of 1 mA cm^{-2}. After that, the cells were cycled at 1 mA cm^{-2} and 5 mAh cm^{-2} (Q_C) for 10 cycles and finally stripped to 1 V (Q_S). The average CE is calculated by Equation 1:

$$CE_{avg} = (10\ Q_C + Q_S)/(10\ Q_C + Q_T). \quad (1)$$

Based on this method, the average CE of Ti_3C_2 and $Mo_2Ti_2C_3$ films is 98.8 and 99.0 %, respectively, further demonstrating the more reversible Mg plating/stripping behaviors on $Mo_2Ti_2C_3$ film.

To further verify the utilization of $Mo_2Ti_2C_3$ film for deep cycling magnesium metal batteries, we cycled the Mg//$Mo_2Ti_2C_3$ cell and the Mg//Ti_3C_2 counterpart at 1, 3, 5, 10, and 15 mAh cm^{-2}. Although the Ti_3C_2 film allows stable Mg plating and stripping at capacities from 1 to 10 mAh cm^{-2}, the corresponding cell cannot reversibly cycle at an areal capacity of 15 mAh

cm^{-2} (Figure 3a). Encouragingly, the cell with $Mo_2Ti_2C_3$ film operates stably under all areal capacity conditions with flat voltage profiles (Figure 3b). Figure 3c shows the average CE can reach as high as 99.3% when the capacity is increased to 15 mAh cm^{-2}. The superiority of $Mo_2Ti_2C_3$ film is also evaluated in the full cell configuration coupling with pre-magnesized Mo_6S_8 cathodes in Figure S11 (Supporting Information). The $Mo_2Ti_2C_3$//Mo_6S_8 cell mostly maintains its initial capacity after 40 cycles, whereas the Ti_3C_2//Mo_6S_8 cell shows continuous capacity fading over 40 cycles. These results further highlights that the $Mo_2Ti_2C_3$ MXene film can serve as a promising current collector for deeply rechargeable Mg metal batteries.

Notably, the extraordinary Mg plating/stripping performance of $Mo_2Ti_2C_3$ film, especially in terms of ultra-large cycling capacity (15 mAh cm^{-2}), outperforms all the reported 3D current collectors for metallic Mg (Figure 3d and Table S1, Supporting Information), such as vertically aligned nickel hydroxide nanosheet arrays grown on carbon cloth ($Ni(OH)_2$@CC, 4 mAh cm^{-2}), Cu mesh with silver nanoparticles (Ag@Cu mesh, 8 mAh cm^{-2}),[12b] graphitic carbon nano-substrates (GC-NSs, 1 mAh cm^{-2}),[12c] porous carbon nanofibers with gold nanoparticles (Au@PCNF, 8 mAh cm^{-2}),[12d] Ag nanoparticles decorated Cu foams (ACF, 5 mAh cm^{-2}),[12e] and vertically aligned N- and O-doped carbon nanofiber arrays on carbon cloth (VNCA@C, 5 mAh cm^{-2})[13]. Given that a 0.1 mm thick commercial Mg foil has a capacity of 38.33 mAh cm^{-2}, deep cycling of Mg metal anode in the asymmetrical cell at 15 mAh cm^{-2} leads to a practical electrode volumetric capacity of 1500 mAh cm^{-3}, far exceeding the theoretical specific capacity of commercial graphite anode (818 mAh cm^{-3}). Previously, our group reported a type of high-utilization (75%) and large-capacity (2874 mAh cm^{-3}) composite magnesium metal anodes, which were constructed by plating metallic Mg on Au nanoparticle-modified commercial Cu foils. However, the actual battery cycling capacity was only 3.75 mAh cm^{-2} and Au nanocoating compromises the cost-effectiveness of magnesium metal batteries.[25] In this regard, the freestanding $Mo_2Ti_2C_3$ MXene film holds great promise for practical application in high-energy-density Mg metal batteries.

The surface chemistries of Ti_3C_2 and $Mo_2Ti_2C_3$ films were studied after the Aurbach CE test in the stripped state to corroborate their different electrochemical performances. SEM images in Figure 4a, b, and Figure S12 (Supporting Information) display large residual magnesium particles on Ti_3C_2 film surface, which accounts for the efficiency loss during cycling. In contrast, the surface of cycled $Mo_2Ti_2C_3$ film presents a smooth surface morphology without large residual inactive Mg particles (Figure 4c, d, Figure S13 and S14 Supporting Information), suggesting its good structural stability during repeated plating/stripping processes. Time-of-flight secondary ion mass spectrometry (TOF-SIMS) characterization was also applied to visualize the surface state of Ti_3C_2 and $Mo_2Ti_2C_3$ films after cycling. Figure 4e and f display the 3D view of the individual distribution of MgO_2^-, MgS^-, MgF^-, $MgCl^-$, $CF_3SO_3^-$ and $C_2H_3O^-$ fragments, indicating the presence of MgO, MgS, MgF_2, $MgCl_2$, some electrolyte residues, and organic oligomers on the surface of Ti_3C_2 and $Mo_2Ti_2C_3$ films after cycling.[10b, 25a] Notably, all these fragments detected on the $Mo_2Ti_2C_3$ film appear with weaker signals compared to those observed on the bare Ti_3C_2 film. The high-resolution F 1s XPS spectra (Figure S15, Supporting Information) further confirm that the formation of MgF_2 is suppressed on the surface of $Mo_2Ti_2C_3$ film. All these characterizations highlight the advantages of $Mo_2Ti_2C_3$ film in suppressing electrolyte decomposition and dead Mg formation during cycling, which account for the superior reversibility of the Mg plating/stripping process.

3. Conclusion

In summary, we demonstrated a freestanding $Mo_2Ti_2C_3$ film using a facile vacuum filtration method with favorable electro-chemo-mechanical properties that efficiently improve electrochemical reversibility, especially the deep cycling performance of Mg metal batteries. The $Mo_2Ti_2C_3$ film possesses desirable surface terminations (more -O, and less -F) in comparison to the Ti_3C_2 film, which not only regulates metallic Mg nucleation, but also inhibits side reactions during long-term operation. Moreover, the superior electrical conductivity and

high mechanical strength of $Mo_2Ti_2C_3$ film result in low charge transfer resistances and mitigate large volume changes in the case of high cycling capacity. Consequently, the $Mo_2Ti_2C_3$ film displays reversible Mg plating/stripping behavior with high Coulombic efficiency of 99.3% at a record-high capacity of 15 mAh cm^{-2}. The demonstration of $Mo_2Ti_2C_3$ film offers a new perspective for designing current collectors with high electrical conductivity, superior mechanical strength, and good electrochemical stability for rechargeable Mg metal batteries. This work also opens a new direction for implementing bimetallic MXene materials in other electrochemical energy storage and conversion devices.

Supporting Information

Supporting Information is available from the Wiley Online Library or from the author.

Acknowledgements

Y. L. and W. Y. L. contributed equally to this work. Z. W. S. acknowledges the Agency for Science, Technology and Research (Central Research Fund Award). H. Y. Y. acknowledges the Singapore Ministry of Education academic research grant Tier 2 (MOE2019-T2-1-181). Q. Z. was supported by the Beijing Natural Science Foundation (2192029), the Science and Technology Major Project of Hebei Province (22284402Z), the National Key Research and Development Program of China (2017YFB0702100), the National Natural Science Foundation of China (11404017), the Technology Foundation for Selected Overseas Chinese Scholars, and the Ministry of Human Resources and Social Security of China. The authors thank Tzee Luai Meng for assistance in nano-indentation tests.

Conflict of Interest

The authors declare no conflict of interest.

References

[1] a) Y. Liang, H. Dong, D. Aurbach, Y. Yao, *Nat. Energy* **2020**, *5*, 1646-656; b) Y. Sun, F. Ai, Y. C. Lu, *Small* **2022**, *18*, 2200009; c) R. Attias, M. Salama, B. Hirsch, Y. Goffer, D. Aurbach, *Joule* **2019**, *3*, 27-52; d) Z. Zhang, S. Dong, Z. Cui, A. Du, G. Li, G. Cui, *Small Methods* **2018**, *2*, 1800020.

[2] a) W. Zhao, Z. Pan, Y. Zhang, Y. Liu, H. Dou, Y. Shi, Z. Zuo, B. Zhang, J. Chen, X. Zhao, X. Yang, *Angew. Chem.* **2022**, *134*, e202205187; b) Z. Zhao-Karger, R. Liu, W. Dai, Z. Li, T. Diemant, B. P. Vinayan, C. Bonatto Minella, X. Yu, A. Manthiram, R. J. Behm, M. Ruben, M. Fichtner, *ACS Energy Lett.* **2018**, *3*, 2005-2013; c) K. Tang, A. Du, S. Dong, Z. Cui, X. Liu, C. Lu, J. Zhao, X. Zhou, G. Cui, *Adv. Mater.* **2020**, *32*, 1904987.

[3] a) J. Xiao, X. Zhang, H. Fan, Y. Zhao, Y. Su, H. Liu, X. Li, Y. Su, H. Yuan, T. Pan, Q. Lin, L. Pan, Y. Zhang, *Adv. Mater.* **2022**, *34*, 2203783; b) J. Bae, H. Park, X. Guo, X. Zhang, J. H. Warner, G. Yu, *Energy Environ. Sci.* **2021**, *14*, 4391-4399; c) A. Y. S. Eng, C. B. Soni, Y. Lum, E. Khoo, Z. Yao, S. K. Vineeth, V. Kumar, J. Lu, C. S. Johnson, C. Wolverton, Z. W. Seh, *Sci. Adv.* **2022**, *8*, eabm2422.

[4] a) D.-T. Nguyen, A. Y. S. Eng, R. Horia, Z. Sofer, A. D. Handoko, M.-F. Ng, Z. W. Seh, *Energy Storage Mater.* **2022**, *45*, 1120-1132; b) D.-T. Nguyen, A. Y. S. Eng, M.-F. Ng, V. Kumar, Z. Sofer, A. D. Handoko, G. S. Subramanian, Z. W. Seh, *Cell Rep. Phy. Sci.* **2020***, 1, 100265*.

[5] a) R. Horia, D. T. Nguyen, A. Y. S. Eng, Z. W. Seh, *Nano Lett.* **2021**, *21*, 8220-8228; b) Y. Sun, Q. Zou, W. Wang, Y.-C. Lu, *ACS Energy Lett.* **2021**, *6*, 3607-3613.

[6] a) H. Dong, O. Tutusaus, Y. Liang, Y. Zhang, Z. Lebens-Higgins, W. Yang, R. Mohtadi, Y. Yao, *Nat. Energy* **2020**, *5*, 1646-656; b) W. Ren, D. Wu, Y. NuLi, D. Zhang, Y. Yang,

Y. Wang, J. Yang, J. Wang, *ACS Energy Lett.* **2021**, *6*, 3212-3220.

[7] S. Hou, X. Ji, K. Gaskell, P.-F. Wang, L. Wang, J. Xu, R. Sun, O. Borodin, C. Wang, *Science* **2021**, *374*, 172-178.

[8] a) Y. Zhao, A. Du, S. Dong, F. Jiang, Z. Guo, X. Ge, X. Qu, X. Zhou, G. Cui, *ACS Energy Lett.* **2021**, *6*, 2594-2601; b) R. Lv, X. Guan, J. Zhang, Y. Xia, J. Luo, *Nat. Sci. Rev.* **2020**, *7*, 333-341.

[9] C. Wang, Y. Huang, Y. Lu, H. Pan, B. B. Xu, W. Sun, M. Yan, Y. Jiang, *Nano-Micro Lett.* **2021**, *13*, 195.

[10] a) S. B. Son, T. Gao, S. P. Harvey, K. X. Steirer, A. Stokes, A. Norman, C. Wang, A. Cresce, K. Xu, C. Ban, *Nat. Chem.* **2018**, *10*, 532-539; b) Y. Zhang, J. Li, W. Zhao, H. Dou, X. Zhao, Y. Liu, B. Zhang, X. Yang, *Adv. Mater.* **2021**, *34*, 2108114.

[11] a) K. M. Janna Eaves-Rathert, Murtaza Zohair, and Cary L. Pint, *Joule* **2020**, *4*, 1324-1336; b) J. H. Kwak, Y. Jeoun, S. H. Oh, S. Yu, J.-H. Lim, Y.-E. Sung, S.-H. Yu, H.-D. Lim, *ACS Energy Lett.* **2021**, *6*, 162-170.

[12] a) J. Liu, J. Zhang, Z. Zhang, A. Du, S. Dong, Z. Zhou, X. Guo, Q. Wang, Z. Li, G. Li, G. Cui, *ACS Nano* **2022**, *16*, 9894-9907; b) F. Wang, D. Wu, Y. Zhuang, J. Li, X. Nie, J. Zeng, J. Zhao, *ACS Appl. Mater. Interfaces* **2022**, *14*, 31148-31159; c) H. D. Lim, D. H. Kim, S. Park, M. E. Lee, H. J. Jin, S. Yu, S. H. Oh, Y. S. Yun, *ACS Appl. Mater. Interfaces* **2019**, *11*, 38754-38761; d) S. Lee, D. Woo Kang, J. Hwan Kwak, S. Shin, J.-W. Park, S.-H. Yu, H.-G. Jung, B. Gon Kim, H.-D. Lim, *Chem. Eng. J.* **2022**, *431*, 133968; e) J. H. Kwak, S. Shin, Y. Jeoun, Y. Lee, S. Yu, Y. S. Yun, Y.-E. Sung, S.-H. Yu, H.-D. Lim, *J. Power Sources* **2022**, *541*, 231724.

[13] Z. Song, Z. Zhang, A. Du, S. Dong, G. Li, G. Cui, *Adv. Mater.* **2021**, *33*, 2100224.

[14] a) J. Luo, C. Wang, H. Wang, X. Hu, E. Matios, X. Lu, W. Zhang, X. Tao, W. Li, *Adv. Funct. Mater.* **2018**, *29*, 1805946; b) X. He, S. Jin, L. Miao, Y. Cai, Y. Hou, H. Li, K. Zhang, Z. Yan, J. Chen, *Angew. Chem.* **2020**, *59*, 16705-16711; c) M. Han, C. E. Shuck,

R. Rakhmanov, D. Parchment, B. Anasori, C. M. Koo, G. Friedman, Y. Gogotsi, *ACS Nano* **2020**, *14*, 5008-5016; d) K. R. G. Lim, M. Shekhirev, B. C. Wyatt, B. Anasori, Y. Gogotsi, Z. W. Seh, *Nat. Synth.* **2022**, *1*, 601-614.

[15] X. Zhang, R. Lv, A. Wang, W. Guo, X. Liu, J. Luo, *Angew. Chem.* **2018**, *57*, 15028-15033.

[16] D. Zhang, S. Wang, B. Li, Y. Gong, S. Yang, *Adv. Mater.* **2019**, *31*, 1901820.

[17] Q. Chen, Y. Wei, X. Zhang, Z. Yang, F. Wang, W. Liu, J. Zuo, X. Gu, Y. Yao, X. Wang, F. Zhao, S. Yang, Y. Gong, *Adv. Energy Mater.* **2022**, *12*, 2200072.

[18] a) Z. Cao, Q. Zhu, S. Wang, D. Zhang, H. Chen, Z. Du, B. Li, S. Yang, *Adv. Funct. Mater.* **2019**; b) C. Wei, H. Fei, Y. Tian, Y. An, H. Guo, J. Feng, Y. Qian, *Energy Storage Mater.* **2020**, *26*, 223-233; c) F. Zhao, P. Zhai, Y. Wei, Z. Yang, Q. Chen, J. Zuo, X. Gu, Y. Gong, *Adv. Sci.* **2022**, *9*, 2103930; d) J.Luo, E. Matios, H. Wang, X. Tao,W. Li, InfoMat **2020**, *2*, 1057-1076.

[19] a) Z. Du, C. Wu, Y. Chen, Z. Cao, R.g Hu, Y. Zhang, J. Gu, Y. Cui, H. Chen, Y. Shi, J. Shang, B. Li, S. Yang, *Adv. Mater.* **2021**, *33*, 2101473; b) B. Anasori, C. Shi, E. J. Moon, Y. Xie, C. A. Voigt, P. R. C. Kent, S. J. May, S. J. L. Billinge, M. W. Barsoum, Y. Gogotsi, *Nanoscale Horiz.* **2016**, *1*, 227-234; c) B. Anasori, Y. Xie, M. Beidaghi, J. Lu, B. C. Hosler, L. Hultman, P. R. C. Kent, Y. Gogotsi, M. W. Barsoum, *ACS Nano* **2015**, *9*, 9507-9516; d) A. D. Handoko, K. D. Fredrickson, B. Anasori, K. W. Convey, L. R. Johnson, Y. Gogotsi, A. Vojvodic, Z. W. Seh, *ACS Appl. Energy Mater.* **2018**, *1*, 173-180; e) Y. Zhang, J.-M. Cao, Z. Yuan, H. Xu, D. Li, Y. Li, W. Han, L. Wang, *Small* **2022**, *18*, 2202313.

[20] a) J. Halim, K. M. Cook, P. Eklund, J. Rosen, M. W. Barsoum, *Appl. Sur. Sci.* **2019**, *494*, 1138-1147; b) K. R. G. Lim, A. D. Handoko, L. R. Johnson, X. Meng, M. Lin, G. S. Subramanian, B. Anasori, Y. Gogotsi, A. Vojvodic, Z. W. Seh, *ACS Nano* **2020**, *14*, 16140-16155.

[21] a) X. Tang, D. Zhou, P. Li, X. Guo, B. Sun, H. Liu, K. Yan, Y. Gogotsi, G. Wang, *Adv. Mater.* **2020**, *28*, 190673 ; b) H. Shi, M. Yue, C. J. Zhang, Y. Dong, P. Lu, S. Zheng, H. Huang, J. Chen, P. Wen, Z. Xu, Q. Zheng, X. Li, Y. Yu, Z. S. Wu, *ACS Nano* **2020**, *14*, 8678-8688; c) D. Yang, C. Zhao, R. Lian, L. Yang, Y. Wang, Y. Gao, X. Xiao, Y. Gogotsi, X. Wang, G. Chen, Y. Wei, *Adv. Funct. Mater.* **2021**, 31, 2010987.

[22] a) C. Yan, X.-B. Cheng, Y.-X. Yao, X. Shen, B.-Q. Li, W.-J. Li, R. Zhang, J.-Q. Huang, H. Li, Q. Zhang, *Adv. Mater.* **2018**, *30*, 1804461; b) X. Wang, Y. He, S. Tu, L. Fu, Z. Chen, S. Liu, Z. Cai, L. Wang, X. He, Y. Sun, *Energy Storage Mater.* **2022**, *49*, 135-143.

[23] Y. X. Zhan, P. Shi, R. Zhang, X. Q. Zhang, X. Shen, C. B. Jin, B. Q. Li, J. Q. Huang, *Adv. Energy Mater.* **2021**, *11*, 2101654.

[24] a) M.-Q. Zhao, C. E. Ren, M. Alhabeb, B. Anasori, M. W. Barsoum, Y. Gogotsi, *ACS Appl. Energy Mater.* **2019**, *2*, 1572-1578; b) M. Xu, S. Lei, J. Qi, Q. Dou, L. Liu, Y. Lu, Q. Huang, S. Shi, X. Yan, *ACS Nano* **2018**, *12*, 3733-3740.

[25] a) Y. Li, G. Yang, S. Sun, C. Zhang, C. Y. J. Lim, A. J. Y. Wong, W. Y. Lieu, Z. Sofer, M. F. Ng, W. Liu, Z. W. Seh, *Nano Lett.* **2022**, *22*, 6808-6815; b) Y. Li, C. Wang, W. Wang, A. Y. S. Eng, M. Wan, L. Fu, E. Mao, G. Li, J. Tang, Z. W. Seh, Y. Sun, *ACS Nano* **2020**, *14*, 1148-1157.

[26] B. D. Adams, J. Zheng, X. Ren, W. Xu, J.-G. Zhang, *Adv. Energy Mater.* **2018**, *8*, 1702097.

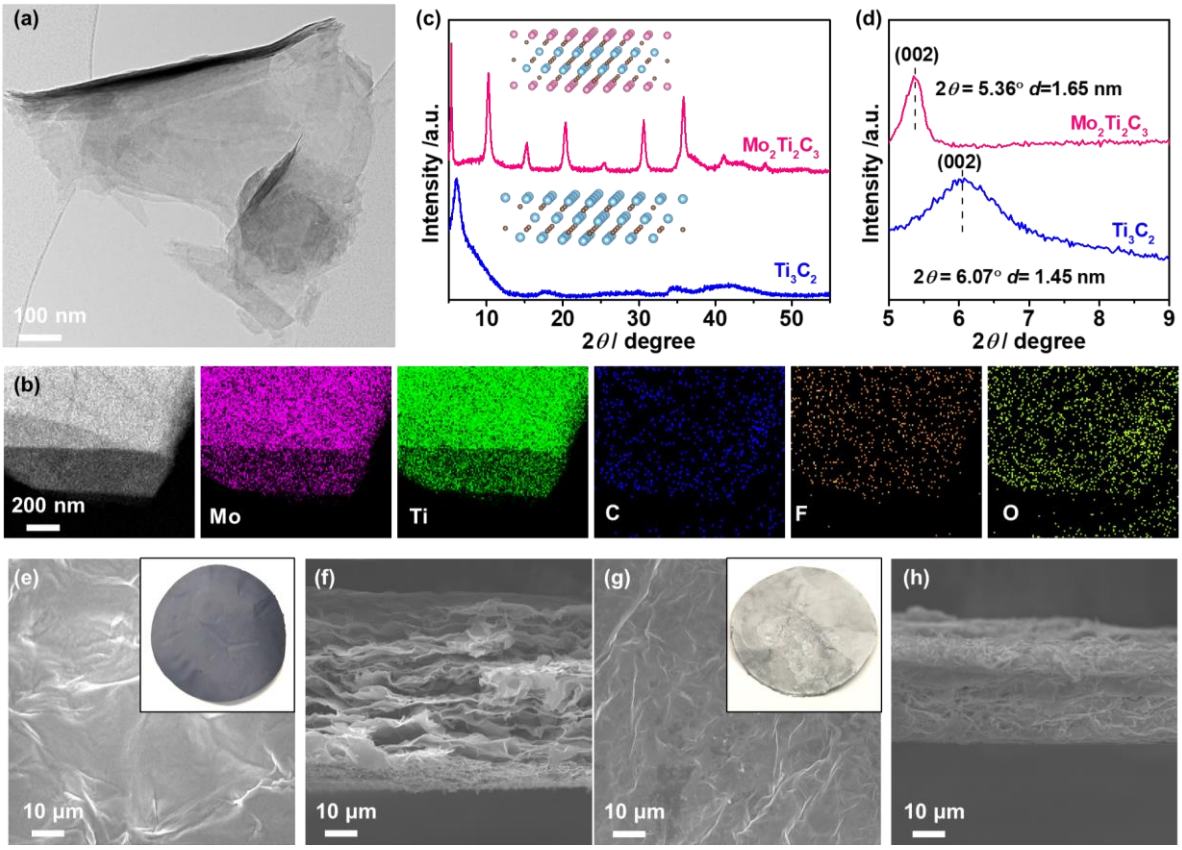

Figure 1 Morphology and chemical composition characterizations of $Mo_2Ti_2C_3$. a) TEM image and b) HAADF-STEM image of $Mo_2Ti_2C_3$ nanosheets and the corresponding elemental mapping images of Mo, Ti, C, F, and O elements, respectively. c, d) XRD patterns and polyhedral representation of Ti_3C_2 and $Mo_2Ti_2C_3$ nanosheets. Mo, Ti and C are depicted in pink, blue and brown, respectively. Optical photographs and SEM images of e, f) Ti_3C_2 and g, h) $Mo_2Ti_2C_3$ films.

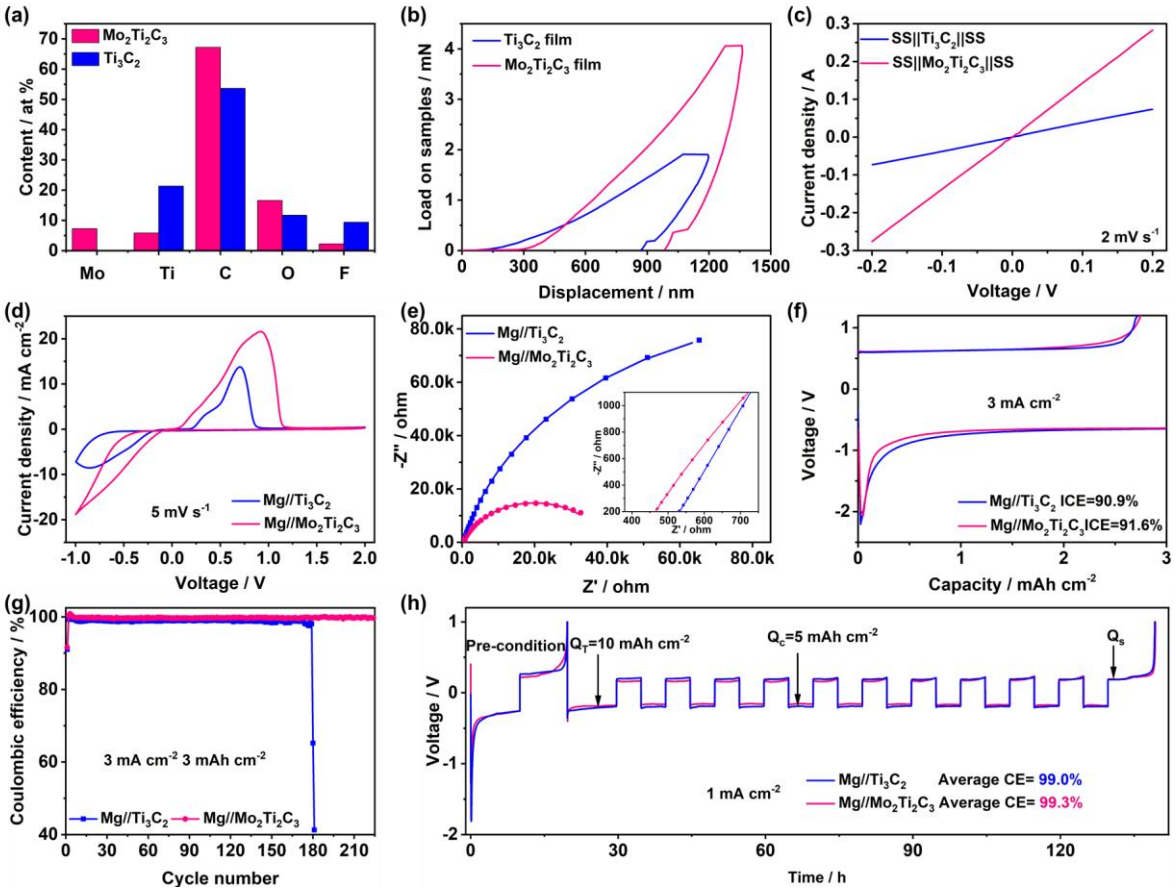

Figure 2 Electro-chemo-mechanical properties of $Mo_2Ti_2C_3$ films. a) Elemental contents obtained by XPS measurement in Ti_3C_2 and $Mo_2Ti_2C_3$ films. b) Force-displacement curves of Ti_3C_2 and $Mo_2Ti_2C_3$ films, measured by a nanoindenter test. c) Polarization I-V curves of symmetric cells with Ti_3C_2 and $Mo_2Ti_2C_3$ films at 2 mV^{-1}. d) CV curves and e) Nyquist plots of Mg//Ti_3C_2 and Mg//$Mo_2Ti_2C_3$ asymmetric cells. f) Initial voltage profiles and g) cycling performances of Mg//Ti_3C_2 and Mg//$Mo_2Ti_2C_3$ asymmetric cells at a current density of 3 mA cm^{-2} and an areal capacity of 3 mAh cm^{-2}. h) The voltage versus time plots of Mg//Ti_3C_2 and Mg//$Mo_2Ti_2C_3$ asymmetric cells during the Aurbach CE test with a current density of 1 mA cm^{-2}.

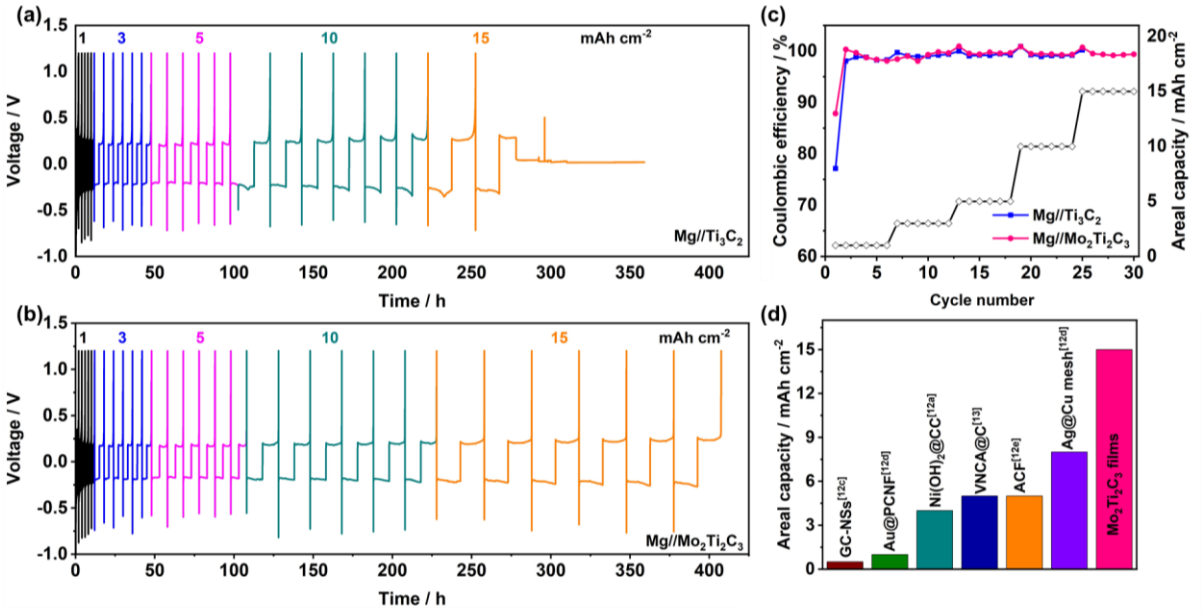

Figure 3 a, b) Voltage profiles and c) Coulombic efficiencies of Mg plating/stripping on Mg//Ti_3C_2 and Mg//$Mo_2Ti_2C_3$ asymmetric cells at a current density of 1 mA cm^{-2} with various areal capacities from 1 to 15 mAh cm^{-2}. d) Performance comparison of our $Mo_2Ti_2C_3$ films with previously reported current collectors for Mg metal anode.

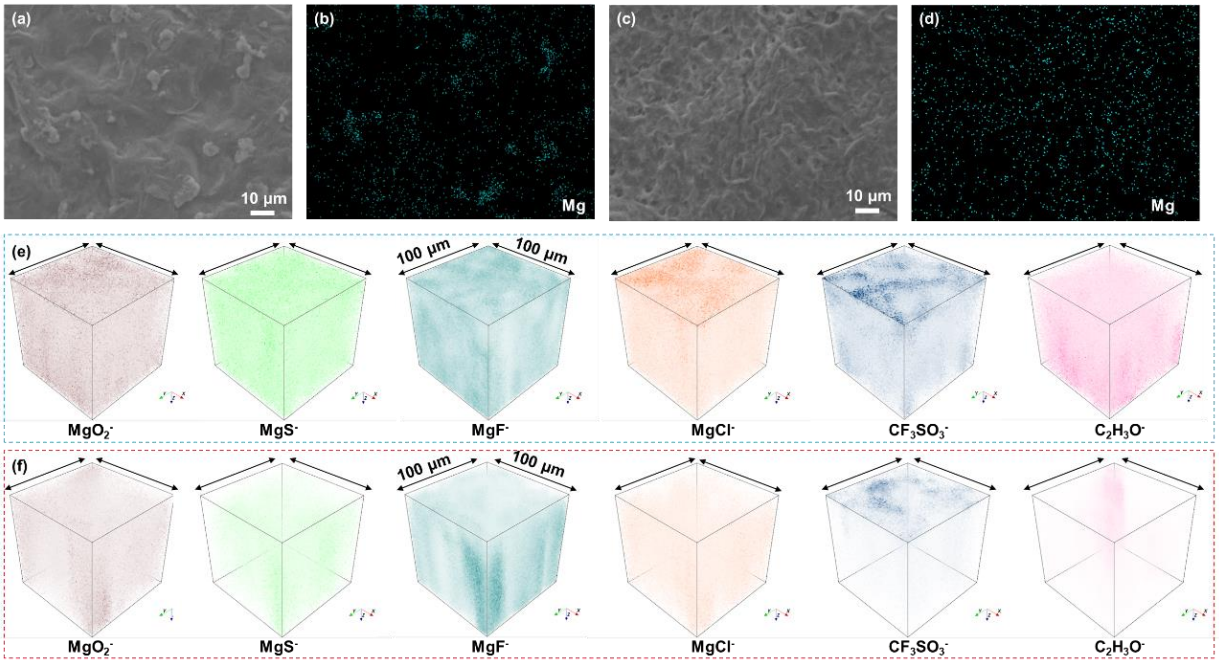

Figure 4 Surface chemistries of the $Mo_2Ti_2C_3$ film after cycling in asymmetric cells. a, c) SEM images, b, d) corresponding elemental mapping, and e, f) TOF-SIMS 3D reconstruction of MgO_2^-, MgS^-, MgF^-, $MgCl^-$, $CF_3SO_3^-$, and $C_2H_3O^-$ fragments for a, b, e) Ti_3C_2 film and c, d, f) $Mo_2Ti_2C_3$ film after the Aurbach CE test.